Spectroscopy of medium-heavy Λ hypernuclei via the (π^+,K^+) reaction

H. Hotchi,[1,*] T. Nagae,[2] H. Outa,[2] H. Noumi,[2] M. Sekimoto,[2] T. Fukuda,[2] H. Bhang,[3] Y. D. Kim,[3,†] J. H. Kim,[3] H. Park,[3,‡] K. Tanida,[1] O. Hashimoto,[4] H. Tamura,[4] T. Takahashi,[4] Y. Sato,[4] T. Endo,[4] S. Satoh,[4] J. Nishida,[4] T. Miyoshi,[4] T. Saitoh,[5] T. Kishimoto,[6] A. Sakaguchi,[6] S. Ajimura,[6] Y. Shimizu,[6] T. Mori,[6] S. Minami,[6] M. Sumihama,[6] R. Sawafta,[7,§] and L. Tang[8]

[1]*Department of Physics, University of Tokyo, Tokyo 113-0033, Japan*
[2]*Institute for Particle and Nuclear Physics, KEK, Tsukuba, Ibaraki 305-0801, Japan*
[3]*Department of Physics, Seoul National University, Seoul 151-742, Korea*
[4]*Department of Physics, Tohoku University, Sendai 980-8578, Japan*
[5]*Laboratory of Nuclear Science, Tohoku University, Sendai 980-0826, Japan*
[6]*Department of Physics, Osaka University, Toyonaka, Osaka 560-0043, Japan*
[7]*Physics Department, North Carolina A&T University, Greensboro, North Carolina 27411*
[8]*Department of Physics, Hampton University, Hampton, Virginia 23668*

(Received 23 April 2001; published 19 September 2001)

Excitation energy spectra of ${}^{89}_{\Lambda}$Y, ${}^{51}_{\Lambda}$V, and ${}^{12}_{\Lambda}$C have been measured via the (π^+,K^+) reaction by using the SKS spectrometer at the K6 beam line in the KEK 12-GeV Proton Synchrotron. In the ${}^{89}_{\Lambda}$Y spectrum, obtained with an energy resolution of 1.65 MeV (FWHM) and in the highest statistics so far, we have succeeded in clearly observing a characteristic fine structure in heavy Λ hypernuclear systems and precisely obtaining a series of Λ single-particle energies in the very wide excitation energy range of more than 20 MeV, for the first time. Also in the ${}^{51}_{\Lambda}$V spectrum, a similar structure to that of ${}^{89}_{\Lambda}$Y was observed. In the ${}^{12}_{\Lambda}$C spectrum, new core-excited states were clearly resolved thanks to the best energy resolution of 1.45 MeV so far achieved by using the SKS spectrometer.

DOI: 10.1103/PhysRevC.64.044302 PACS number(s): 21.80.+a, 25.80.Hp

I. INTRODUCTION

Nuclear systems including strangeness provide us with a unique playground for studying new forms of hadronic many-body systems and various hadronic interactions extended in the flavor SU(3). A hyperon implanted in a nucleus can move around free from the Pauli blocking by nucleons, probing deep inside of the nucleus. Thus hypernuclei can provide invaluable information concerning the behavior of a baryon deep inside a nucleus not accessible in ordinary nuclei. A hypernucleus is also an excellent tool to extract information on the hyperon-nucleon interaction. At this moment, it is not easy to carry out a direct measurement on hyperon-proton scattering at low energy, because it is hard to obtain a high-intensity hyperon beam in this energy due to its short lifetime. Therefore it is a unique opportunity to obtain information on the hyperon-nucleon interaction by observing the fine structures of hypernuclei caused by the specific spin-dependent hyperon-nucleon interactions. For a unified understanding of baryon-baryon interactions in terms of the meson-exchange mechanism and/or the quark-gluon picture, basic experimental data on the hyperon-nucleon interaction as well as the nucleon-nucleon interaction have been long awaited.

Among various hypernuclei, Λ hypernuclei are the most familiar hypernuclear system so far, and allow us to carry out precise spectroscopic investigations thanks to the narrow intrinsic widths [1–3].

In light Λ hypernuclei, in particular, the spin-dependent parts of the Λ-*N* interaction, such as spin-spin, spin-orbit, and tensor interactions, play an important role on the fine level structure. A high energy resolution of much less than 100 keV would be necessary to resolve the fine splittings, because the spin-dependent Λ-*N* interactions are known to be much weaker than those of the *N*-*N* case [4–6]. In this regard, recent attempts at hypernuclear γ-ray spectroscopy appear promising.

On the other hand, heavy Λ hypernuclei can provide us with better information on the behavior of a hyperon in the nuclear medium, because deeper Λ bound states are formed for heavier systems. The basic quantities such as the Λ effective mass and the Λ potential depth in the nuclear medium can be obtained from a series of Λ single-particle energies in the very wide excitation energy range of more than 20 MeV in heavy systems. In astrophysics, it has been discussed that hyperons in the high-density nuclear matter at the core of neutron stars play a significant role in their formation and thermal and structural evolution [7]. They are basic and important parameters for a realistic discussion on various properties of neutron stars. In addition, heavy Λ hypernuclei have significant merit in the measurement of the Λ spin-orbit splitting, because Λ orbits with higher angular momenta, in which the spin-orbit splitting would be enhanced, are bound in going to heavier systems. It is very interesting to compare the splitting enhanced in the higher Λ orbit of heavy Λ hypernuclei with the small splitting in *p*-shell Λ hypernuclei.

*Present address: Brookhaven National Laboratory, Upton, NY 11973.
†Present address: Department of Physics, Sejong University, Seoul 114-747, Korea.
‡Present address: Institute for Particle and Nuclear Physics, KEK, Tsukuba, Ibaraki 305-0801, Japan.
§Present address: TransTech Pharma, Inc., High Point, NC 27265.

The two-body Λ-N spin-dependent interactions may mainly contribute to the splitting in p-shell Λ hypernuclei, while in heavy Λ hypernuclei the splitting due to higher-order many-body effects might contribute additionally.

For a unified understanding of Λ hypernuclear systems, high-quality and systematic spectroscopy is indispensable. However, the existing data are mostly limited to light Λ hypernuclei, and our understanding of heavy Λ hypernuclear systems has been limited by available energy resolution and poor statistics. So far, experimental studies of hypernuclei have been carried out with three major reactions; $(K^-_{\rm stopped},\pi^-)$, in-flight (K^-,π^-), and (π^+,K^+). The production of hypernuclei by the (K^-,π^-) reaction in both stopped and in-flight kaon processes is known to be suitable for light hypernuclear systems in the s and p shells, but not for heavy systems. The (π^+,K^+) reaction was proposed to be an effective tool for investigations of heavy Λ hypernuclei by Thiessen [8] and Dover *et al.* [9] in 1980. This reaction is characterized by a large momentum transfer of 350 MeV/c, which is comparable to the nuclear Fermi momentum. Therefore this reaction efficiently populates configurations with an outer neutron hole and a Λ hyperon in a series of orbits covering all the bound Λ-major shells. In particular, angular-momentum stretched states with maximum spin are selectively excited. The richness of spectroscopic information on Λ hypernuclear bound states obtained in the (π^+,K^+) reaction was demonstrated in experiments at BNL [10–12] and at KEK [13]. In particular, the $^{51}_{\Lambda}$V and $^{89}_{\Lambda}$Y data measured with an energy resolution of 3 MeV [full width at half maximum (FWHM)] at BNL disclosed the independent single-particle nature of a Λ hyperon deep inside a nucleus. Recently, a high-resolution (π^+,K^+) experiment was performed for a wide mass number range of $A=10-208$ by using the SKS spectrometer (KEK-PS E140a [14,15]). One of the surprises in the experiment was the smoothness of the $^{89}_{\Lambda}$Y, $^{139}_{\Lambda}$La, and $^{208}_{\Lambda}$Pb spectra. Each bump structure which reflects the Λ shell structure had a wider width than the energy resolution of 2.3 MeV, and the global shapes were smoother than expected from theoretical calculations. These structures in heavy systems were, in fact, smeared out in the BNL data because of the limited energy resolution. A part of the smoothness could be ascribed to the fragmentation of neutron-hole states due to the complexity of nuclear interactions. For example, one way to explain the smoothness is to enhance the contributions from deep neutron-hole states more than twice to fill up the valleys between the major bumps. However, such a large enhancement does not seem to be reasonable considering the selectivity of the (π^+,K^+) reaction. As another possible way to reproduce the smooth spectral shape, a contribution of the larger spin-orbit splittings than typical values in the Λ orbits was discussed [16]. However, the energy resolution and the statistical significance were not adequate to produce a convincing argument. Thus high quality experimental data on heavy Λ hypernuclei in statistics and energy resolution have been long awaited.

In the present paper, we report on our spectroscopic investigation of medium-heavy Λ hypernuclei, $^{89}_{\Lambda}$Y, $^{51}_{\Lambda}$V, and $^{12}_{\Lambda}$C, via the (π^+,K^+) reaction with the best energy resolution so far achieved by using the SKS spectrometer. In particular, the $^{89}_{\Lambda}$Y spectrum has been measured with an improved energy resolution of 1.65 MeV and about eight times better statistics than that of E140a. In the spectrum, we have succeeded in clearly observing a characteristic fine structure in heavy systems and precisely obtaining a series of Λ single-particle energies in the very wide excitation energy range of more than 20 MeV, for the first time.

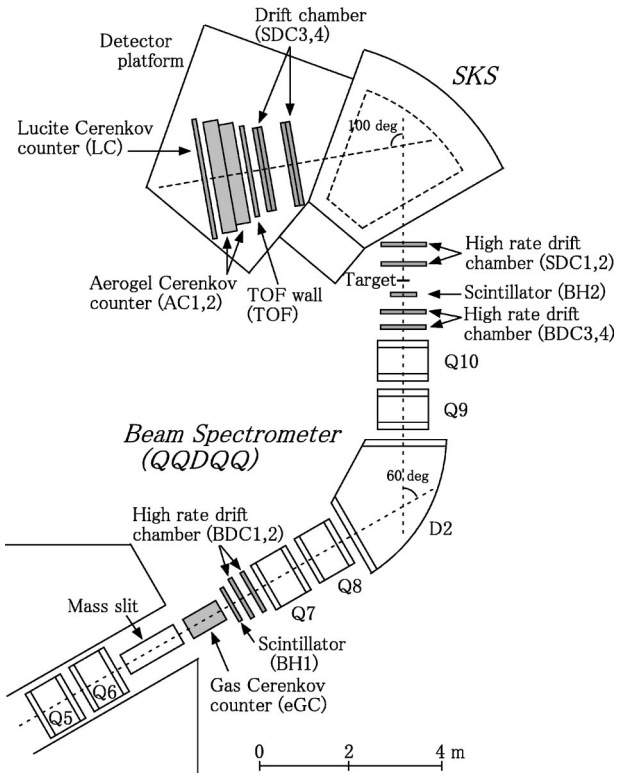

FIG. 1. Schematic view of the experimental setup.

II. EXPERIMENTAL APPARATUS

The experiment (KEK-PS E369) was carried out via the (π^+,K^+) reaction at the K6 beam line in the North Experimental Hall of the KEK 12-GeV Proton Synchrotron using the Superconducting Kaon Spectrometer (SKS). The central momentum of the incident pion beam was set at 1.05 GeV/c. Then, the outgoing kaon was produced with a momentum around 0.72 GeV/c. Figure 1 shows a schematic view of the experimental setup. The incident momentum of the pion was measured with a beam line spectrometer which was comprised of a dipole magnet and four quadruple magnets (QQDQQ), while the momentum of the kaon was measured with the SKS spectrometer which was comprised of a large superconducting dipole magnet. Details of the present detector system are given elsewhere [17]. The two spectrometers were designed to achieve a momentum resolution of 0.1% (FWHM) at 1 GeV/c. Prior to this experiment, the best energy resolution achieved in this spectrometer system was 1.9 MeV for the $(\pi^+,K^+)^{12}_{\Lambda}$C reaction with a 0.9-g/cm^2 carbon target [14]. In the present experiment, the drift-chamber configuration in the SKS spectrometer was modified and also

special care was taken in the drift-chamber position calibrations in the whole spectrometer system in order to reduce systematic errors. Consequently, the energy resolution achieved in the present experiment was 1.45 MeV for the same target, which is significantly better than before.

A. K6 beam line

The K6 beam line is a general-purpose high-intensity beam line that can supply mass-separated secondary beams in the momentum range between 0.5 and 2.0 GeV/c [18]. The secondary pions were produced by the primary 12-GeV proton beam in a platinum production target located at the entrance of the K6 beam line. After momentum and mass selections, the pion beam was achromatically focused on the experimental target. The measured beam size at the experimental target was typically 5.5 mm(horizontal)$\times$8.2 mm (vertical) in rms. The central beam momentum was set at 1.05 GeV/c and its intensity was adjusted to be about 1.5×10^6 per spill at the experimental target.

B. Beam spectrometer

The end part of the K6 beam line was used as a spectrometer in order to analyze the beam momentum. It consisted of a QQDQQ magnet system with four sets of high-rate drift chambers (BDC1–4), a freon-gas Čerenkov counter (eGC), and two sets of segmented plastic scintillation counters (BH1 and BH2).

eGC($n=1.002\,45$) vetoed the positron contamination of 20% in the beam with a rejection efficiency of better than 99.9%. BH1, with seven vertical segments, was installed just downstream of eGC, while BH2, with three vertical segments, was located 30 cm upstream of the experimental target to define the beam hitting the experimental target. By requiring timing coincidence between BH1 and BH2, the proton contamination of 10% in the beam was rejected together with other background particles which could not pass through the QQDQQ system. The beam trigger was defined as BEAM≡BH1×BH2×$\overline{\text{eGC}}$.

In the experiment, we always had the $(\pi^+,K^+)^{12}_{\Lambda}$C events coming from BH2 (72 mm wide, 40 mm high, and 6 mm thick) during the data taking, in addition to the (π^+,K^+) events coming from the target. The $^{12}_{\Lambda}$C spectrum from BH2 was useful for the calibration of the energy scale and the estimation of the energy resolution, as described below.

BDC1–4 (drift space: ±2.5 mm) were installed upstream and downstream of the QQDQQ system. The beam track was measured with a position resolution of 300 μm in rms via BDC's. The beam momentum was obtained particle by particle using a third-order transport matrix calculated with ORBIT [19]. In order to minimize multiple-scattering effects on the momentum resolution, the QQDQQ system was designed so as to make the $\langle x|\theta\rangle$ term of the transport matrix sufficiently small. In addition, the beam pipe in the QQDQQ system was evacuated with a Kapton window of 100 μm thickness, and the drift chambers were made as thin as possible. The magnetic field of the dipole magnet (D2) was monitored during the data acquisition for every spill with a high-precision Hall probe in order to correct its fluctuation in the off-line analysis. The fluctuation was within ±0.05%.

TABLE I. Specifications of the experimental targets. The quoted errors of the thickness come from target size measurements.

Targets	Thickness (g/cm^2)	Purity (%)
^{89}Y	2.223±0.016	99.9
^{51}V	2.816±0.042	99.7
^{12}C	0.859±0.006	99.5
^{12}C	1.739±0.012	99.5

C. SKS spectrometer

The SKS spectrometer, comprised of a superconducting dipole magnet with four sets of drift chambers (SDC1–4) and three kinds of trigger counters (TOF, AC1·2, and LC), was use to analyze scattered particles. This unique apparatus with good momentum resolution (0.1% FWHM) and large acceptance (100 msr) has a short flight path (5 m) to minimize kaon decay and is provided with powerful kaon identification capability.

TOF comprised 15 vertical scintillation counters and was used as a time-of-flight wall for scattered particle identification. A typical timing resolution between BH2 and TOF was 200 ps in rms, which was good enough to separate scattered pions, kaons, and protons. AC1 and AC2 are threshold-type silica aerogel Čerenkov counters ($n=1.06$) for pion veto. LC comprised 14 vertical threshold-type lucite Čerenkov counters ($n=1.49$), and discriminated protons from pions and kaons. The (π^+,K^+) trigger was defined as PIK≡BEAM×TOF×$\overline{\text{AC1}}$×$\overline{\text{AC2}}$×LC. The trigger rate was typically 180 counts for a beam rate of 1.5×10^6 per spill.

SDC1 and SDC2, which were installed at the entrance of the magnet, had the same drift-cell structure as that of BDC's, because they were exposed to the beam. SDC3 and SDC4, which were placed at the exit of the magnet, had a large drift space of ±21 mm. The particle track was measured with a position resolution of 300 μm in rms via SDC's. In the (π^+,K^+) runs, the magnet was excited at 2.2 T (272 A), where the central trajectory corresponded to 0.72 GeV/c. The scattered-particle momentum was obtained particle by particle with the Runge-Kutta method [20] using a precisely measured magnetic field map. In order to reduce multiple scattering effects on the momentum resolution, the drift chambers were made as thin as possible, and the spaces along the particle trajectory were filled with helium bags instead of air. The magnetic field was monitored with an NMR probe during the data acquisition to correct its fluctuation in the off-line analysis. In fact, it was quite stable during the experiment; the fluctuation was within ±0.02%.

D. Experimental targets and data summary

Table I shows specifications of the experimental targets, ^{89}Y, ^{51}V, and ^{12}C (thin and thick), used in the present experiment. The thickness was chosen so as to make the energy-loss straggling sufficiently small in order to keep the energy resolution better than 2 MeV (FWHM). The ^{12}C tar-

TABLE II. Data summary, where N_{beam} is the number of pions incident on each target.

Cycles	Date	Targets	$N_{\mathrm{beam}}(\times 10^9)$
97-1	Nov. 11–16, 1997	^{89}Y	31
		^{12}C	52
97-2	Nov. 19–Dec. 07, 1997	^{89}Y	454
		^{12}C (thin)	41
		^{12}C	83
97-3	Dec. 10–18, 1997	^{89}Y	269
		^{12}C	38
98-1	Jan. 22–31, 1998	^{89}Y	5
		^{12}C	32
98-2	Feb. 06–22, 1998	^{89}Y	134
		^{51}V	144
		^{12}C (thin)	43
		^{12}C	158

gets were used to adjust an absolute energy offset in the binding energy scale and to check the energy resolution; the $^{12}_{\Lambda}$C spectrum is well known to have two well-separated narrow peaks and the width of the ground-state peak directly shows the experimental energy resolution. Also the yield for the $^{12}_{\Lambda}$C ground-state peak was used for checking a stability of the overall detection efficiency.

The data were taken in five separated experimental cycles from November 1997 to February 1998, as listed in Table II. The total number of pions incident on all the targets was about 10^{12}.

III. DATA ANALYSIS

The hypernuclear mass (M_{HY}) is obtained as a missing mass in the (π^+,K^+) reaction as follows:

$$M_{HY}=\sqrt{(E_\pi+M_A-E_K)^2-(p_\pi^2+p_K^2-2p_\pi p_K\cos\theta)}, \tag{3.1}$$

where E_π and p_π are the total energy and momentum of a pion, E_K and p_K are those of a kaon, M_A is the mass of a target nucleus, and θ is the scattering angle of the reaction. Then the binding energy (B_Λ) of a Λ hyperon in the hypernucleus is obtained as

$$B_\Lambda=M_{A-1}+M_\Lambda-M_{HY}, \tag{3.2}$$

where M_{A-1} is the mass of a core nucleus at its ground state and M_Λ is the mass of a Λ hyperon. Thus there were three kinematic variables to be measured via the momentum reconstruction; p_π, p_K, and θ. The procedure of the analysis was comprised of (i) event selection by using the counters' information, (ii) momentum reconstruction for beam particles, (iii) momentum reconstruction for scattered particles, (iv) identification of kaons, (v) reconstruction of the scattering angle and vertex point, and (vi) calculation of the hypernuclear mass.

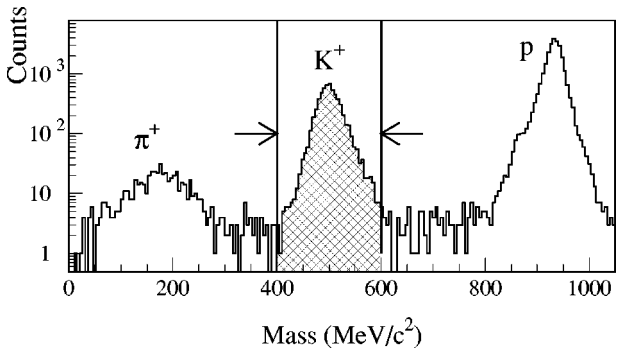

FIG. 2. Scattered-particle mass spectrum obtained for the ^{12}C(π^+,K^+) data. The selected region is shown as arrows.

A. Momentum reconstruction

At the first stage of the analysis, a large background event in the PIK trigger was rejected only using the counters' information. An incident pion was selected by using the time-of-flight information between BH1 and BH2, while a scattered kaon was roughly selected by using the ADC's and TDC's information of TOF and LC. At this stage, the number of events to be analyzed was reduced by about a factor of 10. Then the pion momentum and the kaon momentum were determined by reconstructing particle trajectories from the hit positions in BDC's and SDC's, respectively. In the tracking process, straight-line tracks were first defined locally both at the entrance and the exit of each spectrometer using a least-squares method. Then we assigned the best combination of the straight-line tracks which gave a chi-square minimum in the momentum reconstruction. In the beam spectrometer, a third-order transport matrix was used for the momentum reconstruction, while, in the SKS spectrometer, the momentum was calculated by the Runge-Kutta method with a measured magnetic field map.

B. (π^+,K^+) event selection

The main background in the PIK trigger was fast protons which fired LC, while pions were well suppressed in the trigger level because of the excellent performance of AC1 and AC2. After the momentum reconstruction, the mass of a scattered particle (M_{scat}) was calculated as

$$M_{\mathrm{scat}}=\frac{p}{\beta}\sqrt{1-\beta^2}, \tag{3.3}$$

where β is the velocity of a scattered particle obtained from the time-of-flight measurement between BH2 and TOF, and p is the momentum determined by SKS. Figure 2 shows a typical scattered-particle mass spectrum obtained for the ^{12}C(π^+,K^+) data. Kaons, for which the selected region is indicated with arrows, were clearly separated from pions and protons.

The scattering angle and vertex point were obtained from two tracks; a local straight-line track obtained from BDC3 $\cdot 4$ and a track obtained in the momentum reconstruction of SKS. Figure 3 shows a scatter plot between the horizontal scattering angle and the horizontal position difference of an

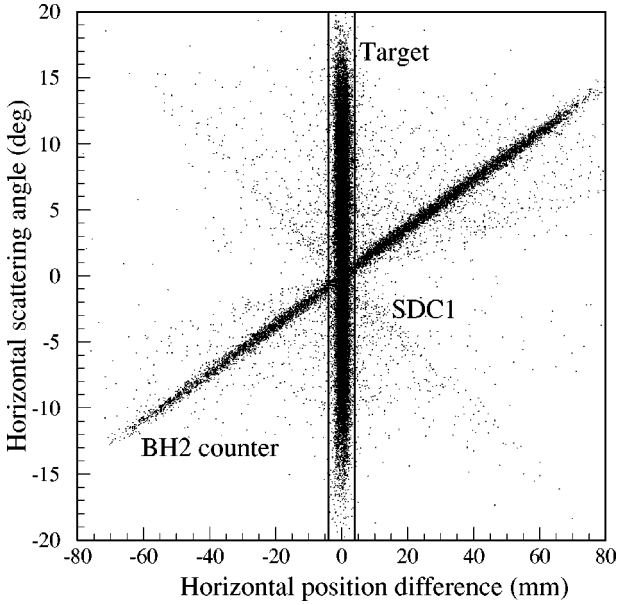

FIG. 3. Scatter plot between the horizontal scattering angle and the horizontal position difference of an incident pion and an outgoing kaon at the target, obtained for the ^{12}C(π^+,K^+) data. The events scattered on the target, BH2, and SDC1 are clearly distinguished as different images.

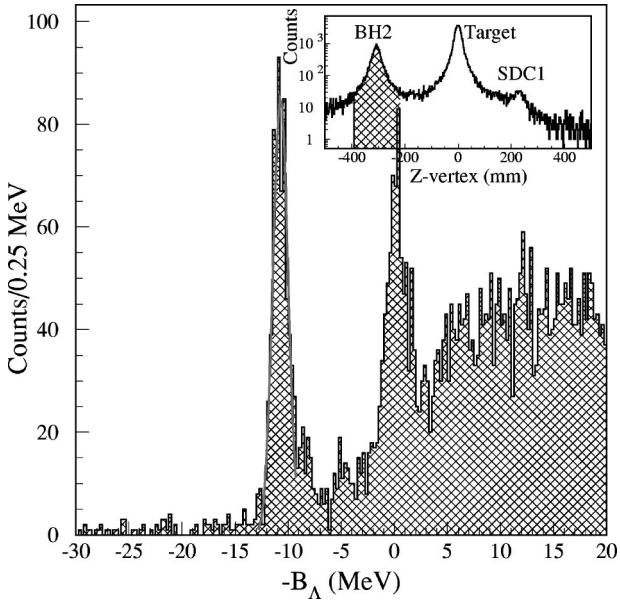

FIG. 4. Mass spectrum in the (π^+,K^+)$^{12}_\Lambda$C reaction on the BH2 counter, obtained at the same time during the ^{89}Y(π^+,K^+) data taking, which was obtained by selecting the hatched region in the inset that shows a *Z* projection (beam direction) of the vertex point.

incident pion and an outgoing kaon at the target point, obtained for the ^{12}C(π^+,K^+) data. In the figure, events scattered on the target, BH2 and SDC1 can be distinguished as different images, and events in the gated region were selected as good events which had a reaction on the target. The backgrounds from BH2 and SDC1 around forward angles were sufficiently rejected by additionally applying the scattering angle cut ($\theta \geqslant 2°$).

C. Energy calibration and precision

In calibrating the binding energy scale, we corrected the kaon momentum so as to adjust the binding energy of the $^{12}_\Lambda$C ground state at 10.76 MeV. This value was taken from the other experimental data obtained in emulsion experiments [21]. As for the $^{89}_\Lambda$Y and $^{51}_\Lambda$V data, the energy scale was adjusted by using the $^{12}_\Lambda$C spectrum from BH2 obtained at the same time during the data taking. As an example, the $^{12}_\Lambda$C spectrum from BH2, which was obtained during the ^{89}Y(π^+,K^+) data taking, is shown in Fig. 4. The validity of the energy calibration with the $^{12}_\Lambda$C spectrum from BH2, located 30 cm upstream of the target, was examined with the ^{12}C(π^+,K^+) data; we checked the consistency between the ground-state peak positions of the $^{12}_\Lambda$C spectra from the carbon target and from BH2. They were consistent within the statistical errors. The binding energy scale was calibrated cycle by cycle within a error of ± 0.17 MeV, which came from a fitting error of the $^{12}_\Lambda$C ground-state peak position.

The linearity of the SKS momentum at 2.2 T was examined by sending pion beams through the two spectrometers at several central momenta from 0.65 to 0.79 GeV/c. The linearity was found to be better than ± 0.04 MeV/c ($\pm 0.04\beta_K$ MeV) in the momentum range. Here we assumed that the central momentum of the beam spectrometer was exactly proportional to the magnetic fields of the beam line magnets.

Taking account of the two errors mentioned above, the total systematic error of the binding energy scale became $\pm\sqrt{(0.04\beta_K)^2+0.17^2}+\Delta E = \pm 0.17 + \Delta E$ MeV for the ^{12}C(π^+,K^+) data, where ΔE is the error based on the definition of the $^{12}_\Lambda$C ground-state binding energy of 10.76 MeV.

As for the other data, the error arising from the energy-loss corrections for pions and kaons based on the calculation should be taken into account additionally. From comparisons between the measured energy losses with pion beams (0.72 and 0.90 GeV/c) and the corresponding calculated values, the error was estimated to be better than ± 0.15 MeV. Thus the total systematic error for the $^{89}_\Lambda$Y and $^{51}_\Lambda$V data was obtained to be $\pm\sqrt{0.17^2+0.15^2}+\Delta E = \pm 0.23 + \Delta E$ MeV.

D. Energy resolution

The experimental energy resolution consists of the momentum resolutions of the two spectrometers and the energy-loss fluctuations in the target and in the BH2 counter. As for the ^{12}C(π^+,K^+) data, the energy resolution was directly obtained by fitting the ground-state peak with a Gaussian form; 1.45 ± 0.06 MeV (FWHM) for the thin target. As shown in Table III, the energy resolution was stable during the experiment.

The energy resolution of the $^{89}_\Lambda$Y spectrum was estimated by using the $^{12}_\Lambda$C spectrum from BH2 obtained at the same time during the data taking. It was calculated to be 1.65 ± 0.10 MeV from the value (1.69 ± 0.10 MeV) directly obtained from the $^{12}_\Lambda$C ground-state peak, by considering the difference of the energy-loss fluctuations in the (π^+,K^+)

TABLE III. Widths and cross sections of the $^{12}_{\Lambda}$C ground-state peak obtained in the different experimental cycles, where the cross sections were obtained in the scattering angles from 2 to 14 ° by integrating the binding energy region from 6.5 to 13 MeV. The quoted errors are statistical.

	Thick target		Thin target	
Cycles	FWHM (MeV)	Cross sections (μb/sr)	FWHM (MeV)	Cross sections (μb/sr)
97-2-1	1.75±0.08	9.6±0.4	1.45±0.09	9.8±0.6
97-2-2	1.77±0.08	10.0±0.4		
97-3	1.74±0.07	10.0±0.4		
98-1	1.72±0.08	9.5±0.5		
98-2-1	1.80±0.06	9.6±0.3	1.48±0.08	9.5±0.6
98-2-2	1.85±0.06	9.1±0.3		

reaction on the target and on BH2. Because the kaons from BH2 also passed through the ^{89}Y target, we could reliably determine the energy resolution for the ^{89}Y(π^+,K^+) reaction. The energy resolution of the $^{51}_{\Lambda}$V spectrum was similarly estimated to be 1.95±0.10 MeV. The validity of the estimation was examined with the ^{12}C(π^+,K^+) data; we checked the consistency between the energy resolution directly obtained from the ^{12}C(π^+,K^+) spectrum and the corresponding resolution estimated from the $^{12}_{\Lambda}$C spectrum from BH2. They were consistent within the statistical errors.

E. Cross section

The cross section was calculated from the experimental yields as

$$\left(\frac{d\sigma}{d\Omega}\right) = \frac{A}{(\rho x)\cdot N_A}\cdot\frac{1}{(N_{\rm beam}\cdot f_{\rm beam})}\cdot\frac{N_K}{\varepsilon_{\rm exp}\cdot d\Omega}, \quad (3.4)$$

where A is the target mass number, ρx the target thickness in g/cm^2, N_A the Avogadro's number, $N_{\rm beam}$ the scaler counts of the BEAM trigger, N_K the number of the (π^+,K^+) events, $d\Omega$ the effective solid angle of SKS, $f_{\rm beam}$ the beam normalization factor, and $\epsilon_{\rm exp}$ represents several experimental efficiency factors; detector and analysis efficiency, data-acquisition efficiency, K^+ decay factor, and K^+ absorption factor.

1. Beam normalization factor

The beam normalization factor represents the fraction of pions in the beam. The positron contamination was rejected with eGC. Also the proton contamination was rejected by requiring timing coincidence between BH1 and BH2. But muons in the beam, which were the decay products of pions, could not be separated from pions. The μ^+ contamination rate was estimated to be 6.2% by using DECAY-TURTLE [22]. The validity of the estimation had been examined in the previous experiment by measuring the contamination rate with a high-pressure freon-gas Čerenkov counter [23]; the calculation agreed with the measurement within ±2.0%.

The accidental coincidence rate between BH1 and BH2 was estimated to be 19.0±0.7% by using the TDC spectrum with the BEAM trigger.

In total, the beam normalization factor was typically 76.0±2.1%.

2. Detector and analysis efficiency

The efficiency in the beam momentum reconstruction was estimated using the BEAM trigger, which was typically 94.5±1.5% in total.

The TOF efficiency was measured to be 99.9±0.1% using a pion beam of 072 GeV/c. The LC efficiency was similarly estimated to be 99.4±0.2%. In the analysis of the counters in SKS, events with more than two hits on TOF or LC were rejected in order to reduce a background level. The corresponding cut efficiency was estimated to be 97.0 ±1.0%.

The efficiency of SDC1·2 including the analysis efficiency was estimated using the BEAM trigger. Since the beam counting rate per wire was quite high at SDC1·2 due to the beam focused at the target, a small degradation of the efficiency was observed near the beam spot. Therefore the efficiency as a function of the horizontal incident position was used for the correction event by event. The averaged value of the SDC1·2 efficiency was typically 91.0±1.5%.

The efficiency of SDC3·4 including the analysis efficiency was estimated using the (π^+,p) events in the PIK trigger because of the negligible decay in flight. Since it had a dependence on the incident position due to some noisy channels, the efficiency as a function of the horizontal incident position was used for the correction event by event. The averaged value of the SDC3·4 efficiency was typically 81.0±1.5%.

The kaon-tracking-χ^2 cut efficiency was estimated to be 97.0±1.4%. The cut efficiency in the kaon identification (the scattered-particle mass cut and the TOF-ADC, LC-ADC, and LC-TDC cuts) was estimated to be 90±1.5% in total. The event-vertex cut efficiency was estimated to be 97.0 ±1.0%.

3. Other factors

The data-acquisition efficiency, caused by the dead time of the data-acquisition system, was determined to be 89.4 ±0.1%.

Due to a high counting rate of AC1·2, some of the PIK triggers were deadened accidentally. The corresponding correction factor was calculated to be 91.5±1.5% from the counting rate (typically 1.5×10^6 s^{-1}) and the coincidence width between AC1·2 and BEAM×TOF×LC(56±5 ns).

The kaon decay rate was studied in detail with a Monte Carlo simulation by T. Hasegawa [23]. The corresponding correction factor was calculated to be 40±2% in typical and it was corrected event by event taking account of the momentum and the flight path length.

The K^+N inelastic cross section is less than 0.5 mb around 0.7 GeV/c [24]. The kaon absorption rate was calculated to be less than 0.4%.

4. Acceptance of the SKS spectrometer

The effective solid angle of SKS ($d\Omega$) was calculated with a Monte Carlo simulation code GEANT [25]. The effects of energy loss and multiple scattering through a trajectory were included in this calculation. The effective solid angle was averaged on the distribution of the beam profile obtained from the experimental data. It was calculated as a function of scattering angle (θ) and momentum (p) as follows:

$$d\Omega(\theta,p)=\int_{\theta-(1/2)\Delta\theta}^{\theta+(1/2)\Delta\theta} d\cos\theta \int_0^{2\pi} d\phi \times \frac{\text{number of events accepted}}{\text{number of events generated}}, \quad (3.5)$$

where events were generated uniformly from $\theta-\frac{1}{2}\Delta\theta$ to $\theta+\frac{1}{2}\Delta\theta$ in the polar angle, from 0 to 2π in the azimuthal angle, and from $p-\frac{1}{2}\Delta p$ to $p+\frac{1}{2}\Delta p$ in the momentum.

5. Total systematic errors

The error on the beam normalization and the experimental efficiency factors was obtained to be $\pm 7\%$ by adding in quadrature assuming no correlations among the factors. As for the effective solid angle of SKS, the possible change caused by the long-term fluctuation of the beam profile was taken into account as a systematic error, which was estimated to be $\pm 1\%$. The error on the target thickness is shown in Table I. The total systematic error on the cross section for each target was obtained combining these errors; $\pm 9\%$ for ${}^{89}_{\Lambda}$Y and ${}^{12}_{\Lambda}$C, and $\pm 10\%$ for ${}^{51}_{\Lambda}$V.

The consistency among the cross sections obtained in the different experimental cycles was examined by using the ^{12}C(π^+,K^+) data. As shown in Table III, the cross sections of the ${}^{12}_{\Lambda}$C ground-state peak, calculated separately for each experimental cycle, agreed quite well within the statistical errors.

F. Background level

The background levels for all the spectra were examined by looking at the events in the region where the binding energy is larger than that for the ground state of a produced Λ hypernucleus. The backgrounds were almost uniform and found to be less than 0.03 μb/sr MeV for all the spectra.

The target-empty (π^+,K^+) data were analyzed using the same analysis program as that for the normal (π^+,K^+) data. The background was almost uniform and estimated to be less than 0.04 μb/sr MeV.

On the basis of the analyses, we assumed the backgrounds around the bound regions of the obtained spectra were negligible and uniform.

IV. EXPERIMENTAL RESULTS

The hypernuclear mass spectra of ${}^{89}_{\Lambda}$Y, ${}^{51}_{\Lambda}$V, and ${}^{12}_{\Lambda}$C (thin target) are shown in Figs. 5, 6, and 7. The vertical scale is shown in the average cross section obtained in the scattering angles from 2 to 14° in the laboratory frame, which is defined as follows:

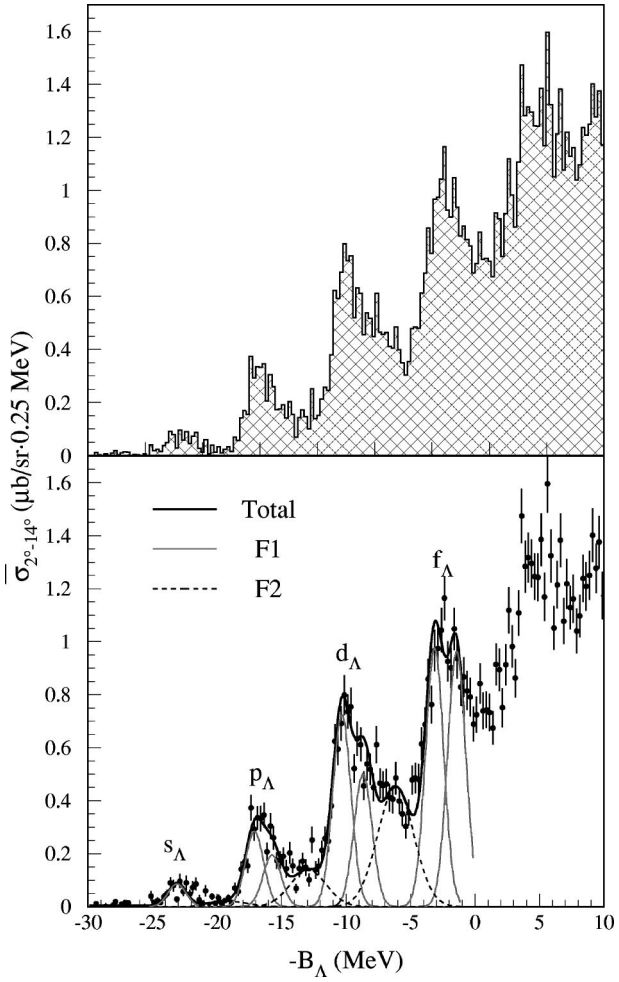

FIG. 5. Hypernuclear mass spectra of ${}^{89}_{\Lambda}$Y without (up) and with (down) fitting curves described in the text. The quoted errors are statistical.

$$\overline{\sigma}_{2°-14°} \equiv \int_{\theta=2°}^{\theta=14°} \left(\frac{d\sigma}{d\Omega}\right) d\Omega \Big/ \int_{\theta=2°}^{\theta=14°} d\Omega. \quad (4.1)$$

The horizontal scale is shown in the binding energy calculated by Eq. (3.2). For convenience, they are shown in the tabular form in Tables IV, V, and VI.

Qualities of the spectra discussed in the last section are summarized in Table VII.

A. ${}^{89}_{\Lambda}$Y

The ${}^{89}_{\Lambda}$Y spectrum showed characteristic bump structures which reflect the major shell structure of the Λ orbits coupled to the $0g_{9/2}^{-1}$ neutron-hole state. The widths for the *p*, *d*, and *f* orbits were significantly wider than expected from the energy resolution of 1.65 MeV (FWHM) and became wider for the Λ orbits with higher angular momenta; the widths were obtained to be 2.4 ± 0.2, 3.0 ± 0.2, and 4.6 ± 0.5 MeV for the *p*, *d*, and *f* orbits by fitting each major bump with a single Gaussian. In particular, the widest bump of the *f* orbit appears to split into two peaks. In the present experiment, the energy resolution can be accurately esti-

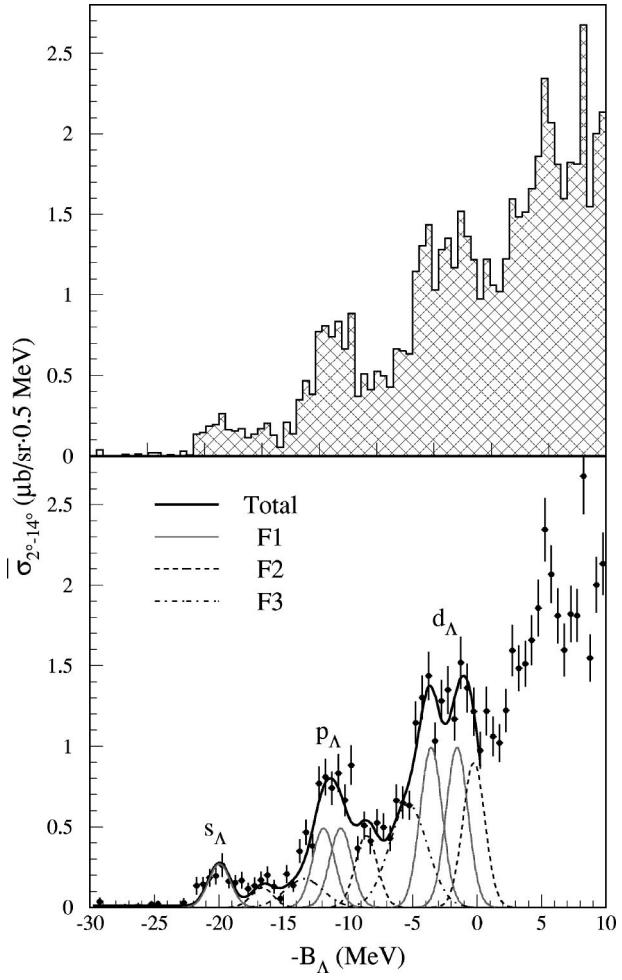

FIG. 6. Hypernuclear mass spectra of $^{51}_{\Lambda}$V without (up) and with (down) fitting curves described in the text. The quoted errors are statistical.

mated by using the $^{12}_{\Lambda}$C spectrum from the BH2 counter obtained at the same time during the data taking, as described in the last section. The large width of the bumps cannot be attributed to the spreading widths, because a series of Λ single-particle states coupled to an outer neutron hole, including even highly excited states, is expected to maintain narrow widths of less than 100 keV [1–3]. Thus we conclude that each of the broad bumps contains at least two peaks.

In between the major bumps, there exist contributions from deeper neutron-hole states such as $0f_{5/2}^{-1}$ and $0f_{7/2}^{-1}$, while contributions from neutron-hole states lying at lower excitation energies, such as $1p_{1/2}^{-1}$ and $1p_{3/2}^{-1}$, would be negligible due to angular momentum mismatch and smaller spectroscopic factors. In fact, in the neutron pickup ^{90}Zr$(p,d)^{89}$Zr reaction [26], it is known that the $0f_{5/2}^{-1}$ and $0f_{7/2}^{-1}$ neutron-hole states are populated at mean excitation energies of 3.27$(5/2^-)$ and 10.3$(7/2^-)$ MeV with intensities of 65–70 % relative to the ground state. However, the contributions from the deep neutron-hole states would be smeared out due to the expected large spreading widths (3–6 MeV). Since they are just located between the major bumps, their contributions should be not so large and almost flat in

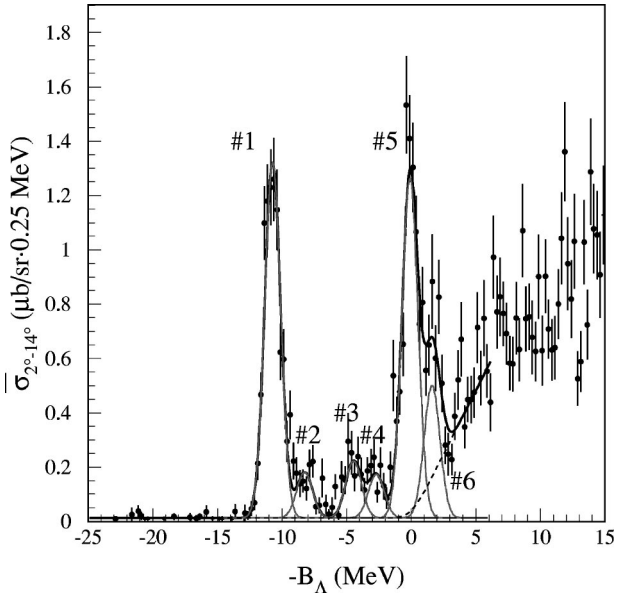

FIG. 7. Hypernuclear mass spectrum of $^{12}_{\Lambda}$C obtained with the thin carbon target. The quoted errors are statistical.

the energy regions near the tops of the major bumps. Therefore the energy regions to be fitted were carefully selected and each of the bumps was fitted with a single Gaussian for the *s* orbit or two Gaussians for the other orbits (F_1), where the Gaussian widths were fixed to be the energy resolution ($\sigma_{\rm exp}$). The whole bound region were fitted well by additionally introducing three Gaussians (F_2) representing extra yields in between the bumps. The fitting function ($F=F_1+F_2$) is written as follows:

$$F_1 = G(a_0,b_0,\sigma_{\rm exp}) + \sum_{l=1}^{3} \{G(a_l^L,b_l^L,\sigma_{\rm exp}) + G(a_l^R,b_l^R,\sigma_{\rm exp})\},$$

$$F_2 = G(A_0,b_0+\delta B,\sigma) + \sum_{l=1}^{2} G(A_l,b_l^L+\delta B,\sigma), \quad (4.2)$$

where $G(a,b,\sigma) \equiv \Delta E_{\rm bin}[(a/\sqrt{2\pi\sigma^2})\exp\{-(x-b)^2/2\sigma^2\}]$ and $\Delta E_{\rm bin}$ is a spectrum bin width. In the fitting, the fitting parameters of F_1 were fixed to be the values obtained from the simple fitting applied to the regions near the tops of the major bumps. The energy shift (δB) from F_1 to F_2 was obtained to be 4.18 ± 0.07 MeV, which was almost consistent with the mean excitation energy of the $5/2^-$ excited state of ^{89}Zr obtained in the neutron pickup ^{90}Zr$(p,d)^{89}$Zr reaction [26]. The results of the fitting are summarized in Table VIII.

B. $^{51}_{\Lambda}$V

The $^{51}_{\Lambda}$V spectrum showed a similar structure to that of the $^{89}_{\Lambda}$Y spectrum. Again, the bumps for the *p* and *d* orbits are significantly wider than expected from the energy resolution of 1.95 MeV (FWHM) and the widths are getting wider as the angular momentum of the Λ orbit increases. The spectrum can be well reproduced in the same way as the $^{89}_{\Lambda}$Y

TABLE IV. List of the data points of the $^{89}_{\Lambda}$Y spectrum shown in Fig. 5. The quoted values of $-B_\Lambda$ show the centers of the bins.

$-B_\Lambda$ (MeV)	$\overline{\sigma}_{2-14^\circ}$ (μb/sr·0.25 MeV)	$-B_\Lambda$ (MeV)	$\overline{\sigma}_{2-14^\circ}$ (μb/sr·0.25 MeV)	$-B_\Lambda$ (MeV)	$\overline{\sigma}_{2-14^\circ}$ (μb/sr·0.25 MeV)	$-B_\Lambda$ (MeV)	$\overline{\sigma}_{2-14^\circ}$ (μb/sr·0.25 MeV)
−29.875	0.000	−19.875	0.033	−9.875	0.736	0.125	0.725
−29.625	0.000	−19.625	0.011	−9.625	0.753	0.375	0.841
−29.375	0.012	−19.375	0.023	−9.375	0.521	0.625	0.739
−29.125	0.003	−19.125	0.033	−9.125	0.633	0.875	0.743
−28.875	0.000	−18.875	0.016	−8.875	0.612	1.125	0.733
−28.625	0.007	−18.625	0.070	−8.625	0.456	1.375	0.674
−28.375	0.000	−18.375	0.057	−8.375	0.538	1.625	0.915
−28.125	0.009	−18.125	0.141	−8.125	0.518	1.875	0.894
−27.875	0.018	−17.875	0.169	−7.875	0.449	2.125	0.751
−27.625	0.003	−17.625	0.155	−7.625	0.611	2.375	0.912
−27.375	0.010	−17.375	0.373	−7.375	0.465	2.625	1.118
−27.125	0.016	−17.125	0.293	−7.125	0.457	2.875	0.982
−26.875	0.014	−16.875	0.335	−6.875	0.463	3.125	0.862
−26.625	0.000	−16.625	0.332	−6.625	0.412	3.375	1.108
−26.375	0.005	−16.375	0.345	−6.375	0.405	3.625	1.473
−26.125	0.003	−16.125	0.207	−6.125	0.485	3.875	1.283
−25.875	0.000	−15.875	0.304	−5.875	0.399	4.125	1.316
−25.625	0.006	−15.625	0.260	−5.625	0.350	4.375	1.295
−25.375	0.000	−15.375	0.174	−5.375	0.303	4.625	1.245
−25.125	0.040	−15.125	0.176	−5.125	0.355	4.875	1.242
−24.875	0.017	−14.875	0.190	−4.875	0.479	5.125	1.385
−24.625	0.023	−14.625	0.142	−4.625	0.485	5.375	1.169
−24.375	0.016	−14.375	0.203	−4.375	0.480	5.625	1.595
−24.125	0.038	−14.125	0.155	−4.125	0.614	5.875	1.323
−23.875	0.049	−13.875	0.069	−3.875	0.687	6.125	1.052
−23.625	0.090	−13.625	0.144	−3.625	0.859	6.375	1.214
−23.375	0.079	−13.375	0.172	−3.375	0.762	6.625	1.383
−23.125	0.028	−13.125	0.148	−3.125	0.967	6.875	1.077
−22.875	0.096	−12.875	0.101	−2.875	0.975	7.125	1.218
−22.625	0.057	−12.625	0.252	−2.625	1.043	7.375	1.129
−22.375	0.090	−12.375	0.139	−2.375	1.164	7.625	1.162
−22.125	0.047	−12.125	0.152	−2.125	0.926	7.875	1.040
−21.875	0.073	−11.875	0.213	−1.875	0.901	8.125	1.096
−21.625	0.086	−11.625	0.257	−1.625	1.048	8.375	1.238
−21.375	0.026	−11.375	0.247	−1.375	0.937	8.625	1.208
−21.125	0.013	−11.125	0.380	−1.125	0.829	8.875	1.250
−20.875	0.060	−10.875	0.624	−0.875	0.867	9.125	1.401
−20.625	0.007	−10.625	0.594	−0.625	0.815	9.375	1.277
−20.375	0.039	−10.375	0.692	−0.375	0.791	9.625	1.376
−20.125	0.014	−10.125	0.799	−0.125	0.689	9.875	1.173

spectrum; we assumed each of the broad bumps was made up of two peaks. In the fitting, the major $0f_{7/2}^{-1}$ neutron-hole state (F_1) and the $0d_{3/2}^{-1}$ and $1s_{1/2}^{-1}$ neutron-hole states (F_2) were assumed to mainly contribute to the spectrum. In fact, in the neutron pickup ^{51}V$(p,d)^{50}$V reaction [27], the $3/2^+$ and $1/2^+$ excited states of ^{50}V are populated at the same excitations of ~3 MeV with a strength of about 30% in total relative to the ground state. The widths of Gaussians corresponding to these neutron-hole states were fixed to be the energy resolution ($\sigma_{\rm exp}$). In addition, we assumed two Gaussians (F_3) representing extra yields from deeper neutron-hole states, where the widths were set to be 3.46 MeV (FWHM) by considering the spreading width. The fitting function ($F=F_1+F_2+F_3$) is expressed as follows:

$$F_1 = G(a_0, b_0, \sigma_{\rm exp}) + \sum_{l=1}^{2} \left\{ G\left(\frac{a_l}{2}, b_l^L, \sigma_{\rm exp}\right) + G\left(\frac{a_l}{2}, b_l^R, \sigma_{\rm exp}\right) \right\},$$

TABLE V. List of the data points of the $^{51}_{\Lambda}$V spectrum shown in Fig. 6. The quoted values of $-B_{\Lambda}$ show the centers of the bins.

$-B_{\Lambda}$ (MeV)	$\overline{\sigma}_{2-14^\circ}$ (μb/sr·0.5 MeV)	$-B_{\Lambda}$ (MeV)	$\overline{\sigma}_{2-14^\circ}$ (μb/sr·0.5 MeV)	$-B_{\Lambda}$ (MeV)	$\overline{\sigma}_{2-14^\circ}$ (μb/sr·0.5 MeV)	$-B_{\Lambda}$ (MeV)	$\overline{\sigma}_{2-14^\circ}$ (μb/sr·0.5 MeV)
−29.75	0.000	−19.75	0.262	−9.75	0.883	0.25	0.975
−29.25	0.035	−9.25	0.163	−9.25	0.367	0.75	1.218
−28.75	0.00	−18.75	0.153	−8.75	0.509	1.25	1.060
−28.25	0.000	−18.25	0.167	−8.25	0.412	1.75	1.020
−27.75	0.000	−17.75	0.115	−7.75	0.526	2.25	1.223
−27.25	0.010	−17.25	0.135	−7.25	0.497	2.75	1.595
−26.75	0.000	−16.75	0.169	−6.75	0.428	3.25	1.485
−26.25	0.014	−16.25	0.200	−6.25	0.665	3.75	1.513
−25.75	0.000	−15.75	0.129	−5.75	0.650	4.25	1.658
−25.25	0.019	−15.25	0.054	−5.25	0.633	4.75	1.859
−24.75	0.021	−14.75	0.207	−4.75	1.147	5.25	2.344
−24.25	0.00	−14.25	0.137	−4.25	1.303	5.75	2.069
−23.75	0.007	−13.75	0.349	−3.75	1.436	6.25	1.810
−23.25	0.000	−13.25	0.466	−3.25	1.032	6.75	1.598
−22.75	0.028	−12.75	0.382	−2.75	1.281	7.25	1.822
−22.25	0.007	−12.25	0.769	−2.25	1.350	7.75	1.812
−21.75	0.135	−11.75	0.809	−1.75	1.168	8.25	2.676
−21.25	0.145	−11.25	0.740	−1.25	1.518	8.75	1.548
−20.75	0.184	−10.75	0.833	−0.75	1.363	9.25	2.003
−20.25	0.195	−10.25	0.665	−0.25	1.216	9.75	2.133

$$F_2 = G(A_0, b_0 + \delta B, \sigma_{\rm exp}) + \sum_{l=1}^{2} G(A_l, b_l^L + \delta B, \sigma_{\rm exp}),$$

$$F_3 = G(A_0', b_0 + \delta B', \sigma) + G(A_1', b_1^L + \delta B', \sigma), \quad (4.3)$$

where, in F_1, the strength ratios between the two peaks in each broad bump were set to be 1:1, and for F_2 and F_3, the strengths were constrained to be (A_l = const × a_l) and (A_l' = const′ × a_l) to that for F_1. The energy shift (δB) from F_1 to F_2 was obtained to be 3.3 ± 0.2 MeV, which was consistent with the excitation energies of the $3/2^+$ and $1/2^+$ excited states of ^{50}V obtained in the neutron pickup ^{51}V$(p,d)^{50}$V reaction [27]. The results of the fitting are given in Table IX.

C. $^{12}_{\Lambda}$C

The $^{12}_{\Lambda}$C spectrum have two prominent peaks at $B_{\Lambda} \approx 11$ and 0 MeV. They were already observed in previous experiments and interpreted as being configurations of $(\nu p_{3/2}^{-1}, \Lambda s)$ and $(\nu p_{3/2}^{-1}, \Lambda p)$ [10–13]. In addition, we have succeeded in clearly resolving four satellite peaks in the spectrum obtained with the thin target, thanks to the best energy resolution of 1.45 MeV (FWHM). The microstructure between the two prominent peaks was discovered in the KEK-PS E140a experiment [14]; two small peaks were observed at 2.6 and 6.9 MeV in the excitation energy, in which the higher one had a broader width than expected from the energy resolution of 2 MeV. In the present experiment, the broad peak was resolved into two peaks.

The spectrum was fitted with six Gaussian peaks (#1–#6) and a quasifree component. In the fitting, the Gaussian widths were constrained to be the same. The quasifree part, representing a continuum spectrum in the unbound region, was fitted with a first order polynomial which is an adequate approximation in the narrow region near $B_{\Lambda} = 0$; it was constrained to be 0 at $B_{\Lambda} = 0$ and folded with the energy resolution. The results of the fitting are listed in Table X.

The angular distributions of the cross sections for the observed peaks were derived from the high-statistics $^{12}_{\Lambda}$C spectrum obtained with the thick carbon target. Though it was unfortunate the small peaks, which were resolved in the thin target data, were somewhat smeared out in the thick target data due to a little worse energy resolution of 1.8 MeV as shown in Fig. 8(a), we fitted it with six Gaussian peaks in the same way as the thin target data. The two results from the thin and thick target data on both excitation energy and cross section were consistent with each other within the statistical errors. The obtained angular distributions are shown in Fig. 8(b) and in Table XI.

V. DISCUSSION

A. $^{89}_{\Lambda}$Y and $^{51}_{\Lambda}$V

1. Structure of heavy Λ hypernuclei

In $^{89}_{\Lambda}$Y, the energy separations ($\delta E_l \equiv b_l^R - b_l^L$) between the two peaks in each broad bump were determined to be 1.37 ± 0.20, 1.63 ± 0.14, and 1.70 ± 0.10 MeV for the *p*, *d*, and *f* orbits. The systematic errors on the energy separations were estimated to be less than ± 0.1 MeV considering two

TABLE VI. List of the data points of the $^{12}_{\Lambda}$C spectrum shown in Fig. 7. The quoted values of $-B_{\Lambda}$ show the centers of the bins.

$-B_{\Lambda}$ (MeV)	$\overline{\sigma}_{2-14^\circ}$ (μb/sr·0.25 MeV)	$-B_{\Lambda}$ (MeV)	$\overline{\sigma}_{2-14^\circ}$ (μb/sr·0.25 MeV)	$-B_{\Lambda}$ (MeV)	$\overline{\sigma}_{2-14^\circ}$ (μb/sr·0.25 MeV)	$-B_{\Lambda}$ (MeV)	$\overline{\sigma}_{2-14^\circ}$ (μb/sr·0.25 MeV)
−24.875	0.000	−14.875	0.008	−4.875	0.294	5.125	0.714
−24.625	0.000	−14.625	0.009	−4.625	0.253	5.375	0.528
−24.375	0.000	−14.375	0.000	−4.375	0.168	5.625	0.748
−24.125	0.000	−14.125	0.000	−4.125	0.239	5.875	0.553
−23.875	0.000	−13.875	0.009	−3.875	0.174	6.125	0.439
−23.625	0.000	−13.625	0.037	−3.625	0.116	6.375	0.972
−23.375	0.000	−13.375	0.000	−3.375	0.186	6.625	0.771
−23.125	0.000	−13.125	0.000	−3.125	0.205	6.875	0.826
−22.875	0.010	−12.875	0.031	−2.875	0.236	7.125	0.765
−22.625	0.000	−12.625	0.022	−2.625	0.108	7.375	0.692
−22.375	0.000	−12.375	0.047	−2.375	0.207	7.625	0.583
−22.125	0.000	−12.125	0.068	−2.125	0.130	7.875	0.580
−21.875	0.000	−11.875	0.214	−1.875	0.086	8.125	0.749
−21.625	0.025	−11.625	0.467	−1.625	0.200	8.375	0.633
−21.375	0.000	−11.375	1.098	−1.375	0.537	8.625	1.071
−21.125	0.037	−11.125	1.179	−1.125	0.369	8.875	0.746
−20.875	0.020	−10.875	1.229	−0.875	0.477	9.125	0.753
−20.625	0.008	−10.625	1.259	−0.625	0.652	9.375	0.677
−20.375	0.008	−10.375	1.147	−0.375	1.533	9.625	0.626
−20.125	0.000	−10.125	0.625	−0.125	1.409	9.875	0.900
−19.875	0.000	−9.875	0.597	−0.125	1.303	10.125	0.628
−19.625	0.000	−9.625	0.294	−0.375	1.065	10.375	0.902
−19.375	0.000	−9.375	0.393	−0.625	0.727	10.625	0.708
−19.125	0.008	−9.125	0.222	−0.875	0.807	10.875	0.631
−18.875	0.000	−8.875	0.178	−1.125	0.556	11.125	0.639
−18.625	0.000	−8.625	0.139	−1.375	0.649	11.375	0.800
−18.375	0.018	−8.375	0.148	−1.625	0.882	11.625	1.042
−18.125	0.000	−8.125	0.122	−1.875	0.601	11.875	1.361
−17.875	0.000	−7.875	0.210	−2.125	0.826	12.125	0.949
−17.625	0.000	−7.625	0.221	−2.375	0.508	12.375	0.819
−17.375	0.000	−7.375	0.054	−2.625	0.281	12.625	1.031
−17.125	0.016	−7.125	0.059	−2.875	0.248	12.875	0.526
−16.875	0.000	−6.875	0.159	−3.125	0.228	13.125	0.589
−16.625	0.011	−6.625	0.062	−3.375	0.387	13.375	1.028
−16.375	0.017	−6.375	0.026	−3.625	0.521	13.625	0.724
−16.125	0.000	−6.125	0.052	−3.875	0.671	13.875	1.287
−15.875	0.034	−5.875	0.128	−4.125	0.348	14.125	1.077
−15.625	0.000	−5.625	0.022	−4.375	0.449	14.375	1.054
−15.375	0.009	−5.375	0.163	−4.625	0.448	14.625	0.908
−15.125	0.000	−5.125	0.152	−4.875	0.475	14.875	1.128

TABLE VII. Characteristics of the hypernuclear mass spectra, where ΔE is the error of the definition of the $^{12}_{\Lambda}$C ground-state binding energy of 10.76 MeV.

Spectra	Target thickness (g/cm^2)	Scattering angle	Systematics			
			Energy precision (MeV)	Energy resolution FWHM (MeV)	Cross section	Background level (μb/sr·MeV)
$^{89}_{\Lambda}$Y	2.22	2−14°	$\pm 0.23 + \Delta E$	1.65 ± 0.10	±9%	<0.02
$^{51}_{\Lambda}$V	2.82	2–14°	$\pm 0.23 + \Delta E$	1.95 ± 0.10	±10%	<0.02
$^{12}_{\Lambda}$C	0.86	2–14°	$\pm 0.17 + \Delta E$	1.45 ± 0.06	±9%	<0.03

TABLE VIII. Results of the fitting for the $^{89}_{\Lambda}$Y spectrum. The quoted errors are statistical.

Peaks ($F1$)	B_Λ (MeV)	FWHM (MeV)	Cross sections (μb/sr)
$l=0$	23.11 ± 0.10	1.65(fixed)	0.60 ± 0.06
$l=1-L$	17.10 ± 0.08		2.00 ± 0.22
$l=1-R$	15.73 ± 0.18		1.38 ± 0.19
$l=2-L$	10.32 ± 0.06		5.10 ± 0.31
$l=2-R$	8.69 ± 0.13		3.52 ± 0.25
$l=3-L$	3.13 ± 0.07		6.87 ± 0.33
$l=3-R$	1.43 ± 0.07		6.79 ± 0.31
Peaks ($F2$)	Energy shift (δB) (MeV)	FWHM (MeV)	Cross sections (μb/sr)
$l=0$	4.18 ± 0.07	3.24 ± 0.15	0.18 ± 0.06
$l=1$			1.83 ± 0.14
$l=2$			6.17 ± 0.28

effects: the possible systematic error in estimating the energy resolution, and the linearity of the energy scale. The fact that the energy separations are getting wider as the angular momentum of the Λ orbit increases suggests that they are due to the spin-orbit splitting. In this regard, the $^{89}_{\Lambda}$Y spectrum was compared with a theoretical one [1,28] based on a distorted-wave impulse approximation (DWIA) calculation with a simple Λ single-particle potential of the Woods-Saxon form, as

$$U_\Lambda(r)=V_0^\Lambda f(r)+V_{LS}^\Lambda(\hbar/m_\pi c)^2\frac{1}{r}\frac{df(r)}{dr}\vec{l}\cdot\vec{s},$$

$$f(r)=\{1+\exp[(r-R)/a]\}^{-1}, \qquad (5.1)$$

TABLE IX. Results of the fitting for the $^{51}_{\Lambda}$V spectrum, where the quoted ratios show the strength ratios of F_2 and F_3 to F_1. The quoted errors are statistical.

Peaks ($F1$)	B_Λ (MeV)	FWHM (MeV)	Cross sections (μb/sr)
$l=0$	19.97 ± 0.13	1.95(fixed)	1.15 ± 0.10
$l=1-L$	11.90 ± 0.17		4.20 ± 0.38(sum)
$l=1-R$	10.57 ± 0.15		(L:R=1:1)
$l=2-L$	3.55 ± 0.14		8.48 ± 0.83(sum)
$l=2-R$	1.55 ± 0.11		(L:R=1:1)
Peaks ($F2$)	Energy shift (δB) (MeV)	FWHM (MeV)	Ratio (A_l/a_l)
	3.31 ± 0.18	1.95(fixed)	0.45 ± 0.06
Peaks ($F3$)	Energy shift ($\delta B'$) (MeV)	FWHM (MeV)	Ratio (A_l'/a_l)
	6.57 ± 0.21	3.46(fixed)	1.13 ± 0.23

TABLE X. Results of the fitting for the $^{12}_{\Lambda}$C spectrum obtained with the thin target, where E_x shows the excitation energy. The quoted errors are statistical.

Peaks	E_x (MeV)	B_Λ (MeV)	Errors (MeV)	FWHM (MeV)	Cross sections (μb/sr)
#1		10.76	(fixed)	1.44 ± 0.05	8.07 ± 0.38
#2	2.51	8.25	±0.17		1.04 ± 0.14
#3	6.30	4.46	±0.11		1.29 ± 0.21
#4	8.06	2.70	±0.19		0.99 ± 0.17
#5	10.66	0.10	±0.04		7.71 ± 0.45
#6	12.37	-1.61	±0.09		3.01 ± 0.40

with the parameters, $V_0^\Lambda=-30$ MeV, $R=1.1(A-1)^{1/3}$ fm, $a=0.60$ fm, and $V_{LS}^\Lambda=4$ MeV, where the strength of the Λ spin-orbit potential (V_{LS}^Λ) of 4 MeV gives rise to the splitting of about 1.5 MeV in the f orbit of $^{89}_{\Lambda}$Y. The global structure

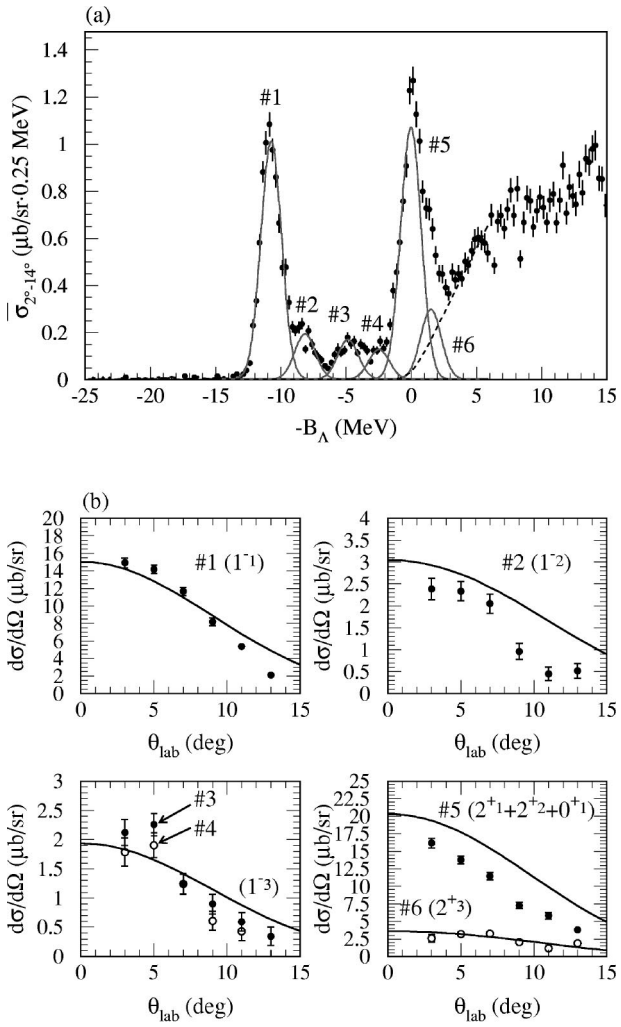

FIG. 8. (a) $^{12}_{\Lambda}$C spectrum obtained with the thick carbon target. (b) Angular distributions of kaons leading to the observed peaks for the ^{12}C(π^+,K^+) reaction, derived from the above high-statistics spectrum. The quoted errors are statistical only. The DWIA calculations by Itonaga are also shown as solid lines.

TABLE XI. List of the differential cross sections for the $^{12}C(\pi^+,K^+)$ reaction shown in Fig. 8(b). The quoted errors are statistical only.

	$d\sigma/d\Omega$ (μb/sr)					
θ_{lab} (deg)	#1	#2	#3	#4	#5	#6
3	14.92±0.56	2.39±0.25	2.12±0.22	1.79±0.24	16.18±0.68	2.59±0.55
5	14.18±0.46	2.34±0.22	2.26±0.19	1.90±0.21	13.76±0.54	3.17±0.46
7	11.66±0.46	2.05±0.22	1.24±0.17	1.24±0.18	11.44±0.54	3.23±0.46
9	8.19±0.44	0.96±0.18	0.90±0.17	0.61±0.16	7.28±0.47	2.02±0.40
11	5.36±0.37	0.45±0.15	0.59±0.16	0.43±0.16	5.83±0.47	1.18±0.35
13	2.11±0.26	0.52±0.17	0.34±0.16	0.05±0.05	3.77±0.44	1.85±0.38

of the experimental spectrum is qualitatively reproduced well by the calculation. However, in careful comparison, the intensity ratios ($R_l \equiv a_l^R/a_l^L$) between the two peaks in each broad bump determined to be 0.69±0.12, 0.69±0.06, and 0.99±0.07 for the *p*, *d*, and *f* orbits from the fitting, were different from those (1, 1.6, and 1.9, respectively) expected in the calculation which were mainly determined from the kinematics of the (π^+,K^+) reaction. The difference could be explained with a small mixing between the two states, $(\nu g_{9/2}^{-1},\Lambda l_{l+1/2})$ and $(\nu g_{9/2}^{-1},\Lambda l_{l-1/2})$, due to some residual interaction [29]. However, we need more detailed theoretical analyses.

A possible alternative would be to interpret the peak on the right side in each Λ orbit as a contribution of a neutron-hole state different from the major $0g_{9/2}^{-1}$ neutron-hole state. In this case, it is a naive expectation that the energy separations (δE_l) would be a fixed amount corresponding to the neutron-hole energy difference. However, the fitting results show the increase of the energy separations for higher angular momenta of the Λ orbits. In addition, the peak intensity ratios (R_l) seem to be too large in this case, because the spectroscopic factors obtained from the neutron pickup $^{90}Zr(p,d)^{89}Zr$ reaction [26] show us that the strength of the $5/2^-$ excited state at 1.46 MeV in the excitation energy is only ~30% relative to the ground state. Therefore it seems that the observed double-peak structures cannot be explained only by the assumption that they are formed from two neutron-hole series.

The $^{51}_{\Lambda}$V spectrum also had a similar structure to that of the $^{89}_{\Lambda}$Y spectrum. The widths of the bumps could be explained in the same way as the $^{89}_{\Lambda}$Y spectrum. Therefore the splitting of Λ orbits with large angular momentum might be a general trend in heavy Λ hypernuclear systems. However, it should be noted that recent hypernuclear γ-ray measurements in $^{13}_{\Lambda}$C and $^{9}_{\Lambda}$Be strongly suggest the two-body Λ-*N* spin-orbit interaction, which causes the Λ single-particle spin-orbit splitting, is too weak to explain the observed structures in $^{89}_{\Lambda}$Y and $^{51}_{\Lambda}$V simply by the spin-orbit splitting [30,31]. The splittings obtained in the present analysis show a somewhat weaker *l* dependence than expected from theoretical calculations, in assuming that the observed double-peak structures are fully originated from the two-body Λ-*N* spin-orbit interaction.

In Table XII, the binding energies and cross sections of the ground states of $^{89}_{\Lambda}$Y and $^{51}_{\Lambda}$V are compared with those obtained from previous (π^+,K^+) experiments at BNL [12] and at KEK [15]. It is noted that the binding energy of the $^{89}_{\Lambda}$Y ground state obtained in the present analysis is about 1 MeV larger than those in the previous data. This apparent difference is understandable by considering that the small yields lying between the *s* and *p* bumps, coming from $1p_{1/2}^{-1}$, $1p_{3/2}^{-1}$, and $0f_{5/2}^{-1}$, are separated from the ground-state peak in the present measurement.

2. Λ effective mass in the nuclear medium

In the present measurement of $^{89}_{\Lambda}$Y, a series of Λ single-particle energies in the very wide excitation energy range of about 24 MeV was obtained with high precision for the first time. The impact of the data was theoretically investigated by Yamamoto [32]. He calculated the Λ single-particle energies of $^{89}_{\Lambda}$Y based on a Brückner-Hartree-Fock-type calculation with density-dependent *G* matrices obtained for two kinds of one-boson exchange potentials (NHC-F and NSC97f [33,34]), assuming the Λ spin-orbit splitting to reproduce the observed double-peak structures. In the calculation, the Λ effective mass (M_Λ^*) at the normal nuclear matter density and the Λ potential depth (U_Λ) are the main parameters to be fitted to reproduce the experimental energy levels. From the fitting, the parameters were obtained to be $M_\Lambda^*/M_\Lambda = 0.72$ and $U_\Lambda = 30.5$ MeV for the case of the

TABLE XII. Comparisons of the obtained binding energies and cross sections of $^{89}_{\Lambda}$Y and $^{51}_{\Lambda}$V ground states with those in previous (π^+,K^+) experiments. The quoted errors of the present results are statistical.

$^{89}_{\Lambda}$Y	B_Λ (MeV)	Cross sections (μb/sr)
Present (2–14°)	23.11±0.10	0.60±0.06
BNL (10°) [12]	22.1±1.6	0.54±0.38
KEK (2–14°) [15]	22.0±0.5	0.21±0.05
$^{51}_{\Lambda}$V	B_Λ (MeV)	Cross sections (μb/sr)
Present (2–14°)	19.97±0.13	1.15±0.10
BNL (10°) [12]	19.9±1.0	1.00±0.56

NHC-F. Similar results were obtained for the case of the NSC97f with slightly different values of $M^*_\Lambda/M_\Lambda = 0.76$ and $U_\Lambda = 30.8$ MeV. The difference between the Λ effective masses is caused by that between the space-exchange parts of the two potentials. Although there still remains a model dependence of the determination of these parameters, the error coming from the experimental data is remarkably small ($\sim \pm 0.01$).

B. $^{12}_{\Lambda}$C

The obtained binding energies and cross sections were compared with a DWIA calculation based on a configuration-mixing shell model [35,36]. In addition to the two prominent peaks, the calculation predicts that two 1^- states and a 2^+ state are populated with non-negligible intensities, which are related to the ^{11}C excited states at 2.0 $(1/2^-)$ and 4.8 $(3/2^-)$ MeV [37]; $(^{11}\mathrm{C}^*_{J=1/2^-} \times \Lambda s)1^-_2$, $(^{11}\mathrm{C}^*_{J=3/2^-} \times \Lambda s)1^-_3$, and $(^{11}\mathrm{C}^*_{J=1/2^-} \times \Lambda p)2^+_3$. The obtained angular distributions of the cross sections are compared with the calculation [38] in Fig. 8(b). The distribution newly obtained for the #6 peak is in good agreement with the calculation. The other distributions are also well reproduced by the calculation except for the #4 peak, as already discussed in the KEK-E336 data [39]. While the theoretical curve (1^-_3) for the #3 peak fits the measured distribution for the #4 peak equally well, the #4 peak is peculiar in terms of the excitation energy. As for the #2, #3, and #6 peaks, the energy shifts from the corresponding core-excitation energies, which reflect the influence of a Λ hyperon on the core nucleus, can be possibly explained with an appropriate Λ-N interaction. However, the energy level of the #4 peak is too high to be explained as a simple core-excited state shifted with conventional Λ-N interactions. A state that can correspond to the #4 peak does not appear within the calculation in the conventional shell-model space.

Recently, an idea of a parity-mixing intershell coupling has been proposed by several theorists [40–43]. In this model, core-nucleus excited states with different parities coupled to different Λ orbits are mixed in $1\hbar\omega$ excited configurations. Although this extended shell-model calculation for $^{12}_{\Lambda}$C is still in progress, it has been reported by Motoba that a new core-excited state can be obtained at the position consistent with the #4 peak [43].

VI. SUMMARY

High quality excitation energy spectra of medium-heavy Λ hypernuclei, $^{89}_{\Lambda}$Y, $^{51}_{\Lambda}$V, and $^{12}_{\Lambda}$C, have been measured via the (π^+, K^+) reaction with the best energy resolution so far achieved by using the SKS spectrometer.

In the $^{89}_{\Lambda}$Y spectrum, characteristic bump structures reflecting the Λ major-shell orbits were clearly observed. The widths for the *p*, *d*, and *f* orbits were significantly wider than expected from the energy resolution of 1.65 MeV (FWHM) and became broader for the Λ orbits with higher angular momenta. In particular, it seems that the widest bump in the *f* orbit split into two peaks. The energy separation in the *f* orbit was determined to be $1.70 \pm 0.10 \pm 0.10$ MeV. The spectrum was reproduced reasonably well assuming that each of the broad bumps was composed of two peaks. From a fitting, a series of Λ single-particle energies from the ground state to the higher ones in the very wide excitation energy range of about 24 MeV was obtained with high precision. The obtained binding energy of the ground state was $\sim$1 MeV larger than those in the previous measurements.

Also in the $^{51}_{\Lambda}$V spectrum, a structure similar to that of $^{89}_{\Lambda}$Y was observed; the bumps for the *p* and *d* orbits were significantly wider than expected from the energy resolution of 1.95 MeV and the widths became broader for the Λ orbits with higher angular momenta. The spectrum was reproduced well in the same way as the $^{89}_{\Lambda}$Y spectrum.

In order to get a clear interpretation on the observed fine structures in heavy Λ hypernuclear systems, further theoretical investigations are necessary.

In the $^{12}_{\Lambda}$C spectrum, new fine structure peaks related to core-excited states were clearly resolved owing to the best energy resolution of 1.45 MeV.

ACKNOWLEDGMENTS

We are grateful to Professor K. Nakamura and the KEK-PS staff for their support of the experiment. We also acknowledge Professor T. Motoba, Professor Y. Yamamoto, Professor K. Itonaga, Professor D. Lanskoy, and Dr. D. J. Millener for valuable discussions on the experimental results. The authors thank Dr. R. E. Chrien and Dr. A. Rusek for a careful reading of this manuscript.

[1] T. Motoba, H. Bandō, R. Wünsch, and J. Žofka, Phys. Rev. C **38**, 1322 (1988).
[2] H. Bandō, T. Motoba, and Y. Yamamoto, Phys. Rev. C **31**, 265 (1985).
[3] A. Likar, M. Rosina, and B. Povh, Z. Phys. A **324**, 35 (1986).
[4] W. Brückner *et al.*, Phys. Lett. **62B**, 481 (1976).
[5] M. May *et al.*, Phys. Rev. Lett. **47**, 1106 (1981).
[6] M. May *et al.*, Phys. Rev. Lett. **51**, 2085 (1983).
[7] M. Prakash and J. U. Lattimen, Nucl. Phys. **A639**, 433c (1998).
[8] H. A. Thiessen, AGS proposal, 758, 1980.
[9] C. B. Dover, L. Ludeking, and G. E. Walker, Phys. Rev. C **22**, 2073 (1980).
[10] C. Milner *et al.*, Phys. Rev. Lett. **54**, 1237 (1985).
[11] R. E. Chrien, Nucl. Phys. **A478**, 705c (1988).
[12] P. H. Pile *et al.*, Phys. Rev. Lett. **66**, 2585 (1991).
[13] M. Akei *et al.*, Nucl. Phys. **A534**, 478 (1991).
[14] T. Hasegawa *et al.*, Phys. Rev. Lett. **74**, 224 (1995).
[15] T. Hasegawa *et al.*, Phys. Rev. C **53**, 1210 (1996).
[16] T. Nagae, in Proceedings of the 23rd INS International Symposium, Tokyo, Japan, 1995, edited by S. Sugimoto and O. Hashimoto, p. 175.

[17] T. Fukuda *et al.*, Nucl. Instrum. Methods Phys. Res. A **361**, 485 (1995).
[18] K. H. Tanaka *et al.*, Nucl. Phys. **A450**, 533c (1986).
[19] S. Morinobu (private communication).
[20] J. Myrhein and L. Bugge, Nucl. Instrum. Methods **160**, 43 (1979).
[21] D. H. Davis, Nucl. Phys. **A547**, 369c (1992).
[22] K. L. Brown *et al.*, CERN 74-02, 1974.
[23] T. Hasegawa, Ph.D. thesis, University of Tokyo, INS-IM-15, 1994.
[24] C. B. Dover and G. E. Walker, Phys. Rep. **89**, 1 (1982).
[25] CERN Program Library Entry W5013, GEANT.
[26] J. Kasagi *et al.*, Phys. Rev. C **28**, 1065 (1983).
[27] H. Ohmura *et al.*, Phys. Lett. **73B**, 145 (1978).
[28] T. Motoba, in Proceedings of the 23rd INS International Symposium (Ref. [16]), p. 187.
[29] D. E. Lanskoy (private communication).
[30] A. Sakaguchi, in *Proceedings of the APCTP Workshop on Strangeness Nuclear Physics (SNP'99)*, Seoul, Korea, 1999, edited by Il-T. Cheon, S. W. Hong, and T. Motoba (World Scientific, Singapore, 2000), p. 231.
[31] H. Tamura *et al.*, Nucl. Phys. **A663**, 481 (2000).
[32] Y. Yamamoto, in *Proceedings of the APCTP Workshop on Strangeness Nuclear Physics (SNP'99)* (Ref. [30]), p. 60.
[33] M. M. Nagels, T. A. Rijken, and J. J. deSwart, Phys. Rev. D **20**, 1633 (1979).
[34] T. A. Rijken, V. G. J. Stoks, and Y. Yamamoto, Phys. Rev. C **59**, 21 (1999).
[35] K. Itonaga, T. Motoba, and H. Bandō, Prog. Theor. Phys. **84**, 291 (1990).
[36] K. Itonaga, T. Motoba, O. Richter, and M. Sotona, Phys. Rev. C **49**, 1045 (1994).
[37] F. Ajzenberg-Selove, Nucl. Phys. **A248**, 1 (1975).
[38] K. Itonaga (private communication).
[39] T. Takahashi *et al.*, Nucl. Phys. **A670**, 265 (2000).
[40] D. J. Millener, in *New Vistas in Physics with High-Energy Pion Beams*, edited by B. F. Gibson and J. B. McClelland (World Scientific, Singapore, 1993), p. 19.
[41] A. Gal, in Proceedings of the 23rd INS International Symposium (Ref. [16]), p. 23.
[42] L. Majling *et al.*, Phys. Part. Nucl. **28**, 101 (1997).
[43] T. Motoba, Nucl. Phys. **A639**, 135c (1998).